Energy Engineering

Tech Science Press

https://doi.org/10.32604/ee.2026.079043

ARTICLE

Coordinated Optimization Strategy for Hybrid Energy Storage toward High-PV-Penetration Distribution Networks

Yechun Xin[1], Xinxin Cheng[1], Yanxu Wang[1,*], Weiru Wang[1], Jiexiang Han[2] and Zhen Niu[3]

[1]School of Northeast Electric Power University, Key Laboratory of Modern Power System Simulation and Control & New Technology, Ministry of Education, Jilin, China

[2]State Grid Corporation of Gansu Province, Lanzhou, China

[3]Electric Power Science Research Institute, State Grid Corporation of Gansu Province, Lanzhou, China

*Corresponding Author: Yanxu Wang. Email: yxwang@neepu.edu.cn

Received: 13 January 2026; Accepted: 06 March 2026; Published: 27 April 2026

ABSTRACT: Addressing voltage violations and renewable energy absorption bottlenecks arising from high-penetration photovoltaic (PV) integration, this paper proposes a hierarchical optimisation architecture for a Hybrid Energy Storage System (HESS) based on microgrid-distribution network coordination to enhance collaborative regulation of energy storage across multiple microgrids. The methodology comprises a PV hosting capacity assessment model and an HESS operation model that accounts for power supply reliability, forming a two-layer planning framework that integrates distributed decision-making with centralized coordination. At the microgrid level, HESS capacity is determined to minimise the local comprehensive cost, while the allocation ratio between lithium-based and hydrogen-based energy storage is optimised to maximise renewable energy utilization. At the distribution network level, a global collaborative dispatch of multi-microgrid energy storage is performed to minimise total system cost and voltage deviation, thereby achieving cross-regional power balance and voltage support. Simulation verification is conducted using actual distribution network data from Zhejiang Province and a 33-node test system. The results indicate that the proposed coordinated operation strategy can effectively improve voltage quality, enhance the PV absorption rate, and increase economic benefits.

KEYWORDS: Hybrid energy storage capacity configuration; mayfly algorithm; high proportion of photovoltaics; bi-level optimization

1 Introduction

In light of the ongoing energy transition, the rapid proliferation of distributed energy resources, such as wind and PV power, has emerged as a pivotal trend shaping the future landscape of renewable energy [1–3]. Recently, the large-scale integration of distributed PV (DPV) systems into distribution networks has increased PV penetration [4,5], significantly affecting the secure operation of distribution systems. Major challenges include bidirectional power flow within the distribution network, voltage violations at the extremities of feeder lines, increased line losses, limited PV absorption capacity, and reverse power flow [6]. To mitigate the impacts of PV integration while enhancing utilisation, the deployment of energy storage systems has become a practical solution. These systems can attenuate fluctuations in PV generation, improve power flow within the distribution network, reduce system losses, and prevent issues such as voltage violations and reverse power flow [7]. The primary challenge is determining the optimal configuration of energy storage systems and developing effective dispatch strategies to maximise their performance [8–10].

Currently, the setup of energy storage systems in both distribution networks and microgrids mainly considers two key factors: the inherent uncertainty of distributed generation and the technological features of different storage options [11,12]. The setup process is usually guided by specific operational optimization goals. Most studies focus on a single energy storage technology, configuring it based on operational optimization objectives. In [13], the author focuses on large-scale compressed air energy storage (CAES) power stations, proposing a multi-dimensional relay protection configuration strategy to enhance system security. The analysis examines a single energy storage technology, addressing the protection challenges arising from frequent start-stops and complex electrical structures. In [14], the author optimizes the siting and operation of energy storage through indicator design, achieving cost reduction, voltage improvement, and enhanced flexibility. In [15], an improved crow search algorithm (CSA) co-optimizes WT/PV/ESS siting and sizing, reducing power losses, ESS costs, flicker emissions, and voltage deviation. Validated across three scenarios, joint WT-ESS optimization significantly decreases losses and flicker, with CSAD outperforming benchmarks in accuracy and robustness. However, reliance on a single energy storage technology may limit its ability to address multi-timescale fluctuations and multi-demand scenarios.

Regarding the optimization of hybrid energy storage system capacity in microgrids, domestic and international scholars have conducted relevant research in recent years. In [16], an independent photovoltaic-storage microgrid is used as the research object, aiming to minimize the initial investment cost and to determine the optimal energy storage capacity using valve-regulated lead-acid batteries, lithium-ion batteries, and vanadium redox flow batteries. In [17], the objective is to minimize the investment and operational costs of HESS in DC microgrid clusters, employing both energy-type and power-type energy storage, and proposing an HESS capacity optimization configuration method for microgrid clusters. In [18], a two-stage optimization framework based on a Stackelberg game is proposed, integrating shared energy storage leasing and microgrid coalition (MGCO) collaboration. NSGA-II optimizes storage dispatch, while Stackelberg equilibrium balances benefits among the active distribution network, MGCO, and SESO under time-of-use pricing incentives. In [19], a two-stage optimal dispatch framework coordinates CES and DES for RES fluctuation smoothing, with a consensus algorithm dynamically optimizing DES power allocation to minimize lifespan decay costs. In [20], a bi-level optimization model for a microgrid with HESS, considering battery life, is constructed, achieving a 13.64% reduction in economic costs for users. However, the aforementioned studies typically focus only on the local microgrid perspective, addressing the source-load imbalance caused by PV grid integration through optimal HESS configuration. They neglect the electrical coupling and power interactions among microgrids.

To enhance the photovoltaic hosting capacity and power supply quality of a multi-microgrid distribution system with high distributed PV penetration, this paper first establishes the global architecture of a distribution network comprising multiple microgrids and the local architecture of a microgrid with a lithium-hydrogen hybrid energy storage system (HESS). Subsequently, models are developed for PV grid-integration load characteristics, accounting for voltage deviation, and for the HESS, reflecting power supply requirements. A bi-level hybrid energy storage optimisation configuration model is then formulated, comprehensively considering voltage deviation, improvement in the absorption rate, and construction and operational economics. At the microgrid level, the Mayfly Algorithm (MA) is used to coordinate multiple energy storage technologies. The HESS capacity is configured to minimise the local comprehensive cost, and the allocation ratio between lithium-based and hydrogen-based energy storage is optimised to maximise renewable energy utilisation. At the distribution network level, distributed stochastic gradient descent (SGD) is used to coordinate the global operational balance of multi-microgrid participation in the grid, with objectives of minimising total cost and voltage deviation. Finally, case studies verify the feasibility and effectiveness of the proposed strategy in practical applications.

2 Structure

2.1 Modelling the Distribution Network Architecture with Multiple Microgrids

In a distribution network with high PV penetration, a typical multi-microgrid distribution architecture is built based on an actual power grid prototype to facilitate the efficient allocation of energy storage, as shown in Fig. 1. Each microgrid includes PV units, a HESS, local loads, and electric vehicle charging stations. Within the system, each microgrid is equipped with an Independent Decision System (IDS), responsible for collecting and processing local operational data. A Centralized Information Decision System (CIDS) coordinates the optimisation decisions for all microgrids, enabling cooperative management. The microgrid architecture that integrates a lithium–hydrogen HESS mainly comprises distributed generation units, hybrid energy storage, and loads. The primary goals of this hybrid storage microgrid are to maximize PV utilization and reduce overall energy costs. To leverage the advantages of both storage technologies, hydrogen and electrochemical storage are deployed. Hydrogen storage offers large capacity and long discharge duration, suitable for long-term peak shaving and valley filling. Lithium-ion storage provides high power density and quick response, allowing for short-term power regulation. The proposed HESS combines the benefits of lithium-ion batteries and hydrogen storage, offering high-efficiency energy storage along with rapid dynamic response. Additionally, it provides an extended service life and lower maintenance needs.

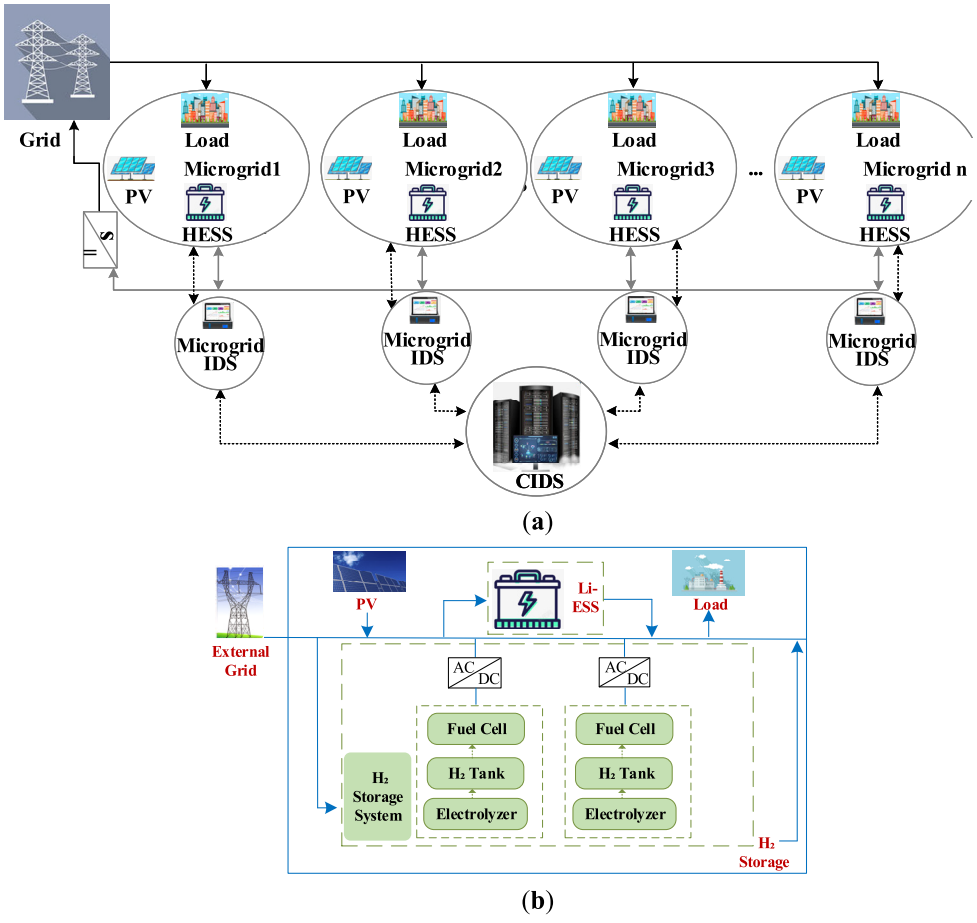

Figure 1: (**a**) Distribution network system architecture with multiple microgrids; (**b**) Microgrid system architecture with lithium-hydrogen hybrid energy storage.

2.2 Analysis and Modeling of DPV Grid-Connected Features

2.2.1 Mechanism of Voltage Deviation Induced by PV Grid Integration

The integration of DPV systems into distribution networks can lead to voltage fluctuations at the point of common coupling. These fluctuations mainly result from two factors: (1) mismatch between PV generation capacity and local load demand, and (2) PV output variability. Fig. 2 illustrates the configuration of multiple DPV systems connected to a common feeder. Assume the distribution line comprises a total of N load nodes. The power consumption at the n-th load node is $P_n + jQ_n$ ($n = 1, 2, 3, \ldots, N$), The voltage at the sending end is U_0, the line impedance between the $(n-1)$-th and n-th nodes is $R_n + jX_n$, and l_n denotes the line length between these two nodes.

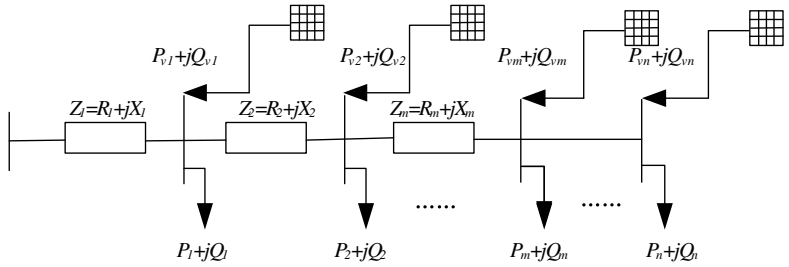

Figure 2: Topology of photovoltaic integration in low-voltage distribution lines.

Before PV integration, the voltage at node m U_{m0} is represented as:

$$U_{m0} = U_0 - \sum_{k=1}^{m} \frac{\sum_{n=k}^{N} P_n r l_k + \sum_{n=k}^{N} Q_n x l_k}{U_{k-1}} \tag{1}$$

The capacity of the DPV system connected to the n-th load node is represented as $P_{vn} + jQ_{vn}$. After integrating the DPV system, the voltage at node m, denoted as U_m, is given by Eq. (2). Neglecting the influence of reactive power, the expression can be simplified as shown in Eqs. (3) and (4).

$$U_m = U_0 - \sum_{k=1}^{m} \frac{\sum_{n=k}^{N} (P_n - P_{vn}) r l_k + \sum_{n=k}^{N} (Q_n - Q_{vn}) x l_k}{U_{k-1}} \tag{2}$$

$$U_{m0} = U_0 - \sum_{k=1}^{m} \frac{\sum_{k=1}^{N} P_n r l_k}{U_{k-1}} \tag{3}$$

$$U_m = U_0 - \sum_{k=1}^{m} \frac{\sum_{n=k}^{N} (P_n - P_{vn}) r l_k}{U_{k-1}} > U_0 - \sum_{k=1}^{m} \frac{\sum_{n=k}^{N} P_n r l_k}{U_{k-1}} \tag{4}$$

After integrating DPV systems, voltages at all nodes along the feeder rise. The degree of this increase depends on factors such as PV output, connection location, and local load demand. When the grid-connected capacity is relatively high, voltage violations may occur near the point of interconnection.

2.2.2 Analysis of Source–Load Matching Traits of Grid-Connected PV Systems

To reveal the load characteristics and operational constraints of high-penetration PV integration into the distribution network, the analysis is based on load time-series matching and capacity-location coordinated planning. Fig. 3 shows a significant mismatch between load and PV time-series coupling. This mismatch is evident in the following aspects:

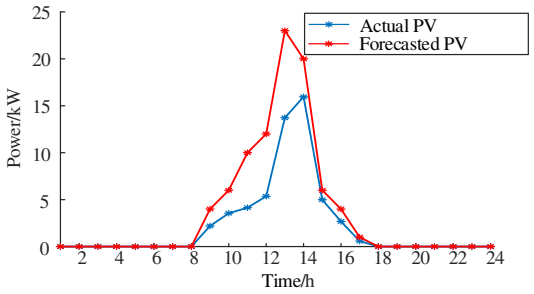

Figure 3: Photovoltaic consumption rate curve of a typical region.

(1) Time-Series Matching Degree: The photovoltaic generation varies greatly with sunlight, causing a mismatch between its time series and the load profile. Some of the PV generation cannot be immediately stored or used. It is important to assess the network's real-time absorption capacity and storage needs.

(2) Power Mismatch Degree: The proportion of periods with power mismatch, denoted as $\varphi(t)$, is calculated as follows:

$$\varphi(t) = \frac{\sum_{t=1}^{T} \rho(t)}{T} \tag{5}$$

where, $T = 96$, $\rho(t)$ is an indicator function that shows whether a power mismatch occurs at time t; the proportion of mismatch periods is 39%. The power mismatch indicates the conflict between the source–load time-series coupling characteristics and the grid's regulation ability, which must be mitigated by accurately planning the capacity and power rating of energy storage systems.

2.2.3 Mechanism Constraints on the Absorption Rate of Grid-Connected Photovoltaics

The PV absorption rate is affected by several constraints, such as PV output characteristics, fluctuations in PV power, and the power flow limits of the distribution network:

$$\eta_{PV} = \frac{P_{PV,net}}{P_{PV,total}} \times 100\% \tag{6}$$

where $P_{PV,net}$ denotes the PV generation power successfully fed into the grid, and $P_{PV,total}$ represents the total generation power of the PV system.

(1) PV Fluctuation Constraint

PV output shows both randomness and volatility. Excessive fluctuation amplitude ΔP_{PV} can cause a temporary mismatch between the grid and energy storage, which hampers PV absorption. It is important to keep ΔP_{PV} within the grid's allowed range.

$$\Delta P_{PV} = \left| P_{PV}(t) - P_{PV}(t-1) \right| \leq \Delta P_{grid,max} \tag{7}$$

(2) Power Balance Constraint

In a distribution network system, a microgrid has the ability to operate independently and can also locally control the flow of electric energy.

$$P_i^{\text{grid}} = P_{\text{PV,net}} + P_i^{\text{HESS}} - P_{\text{load}} \tag{8}$$

In the equation: P_i^{grid} is the power supply from the grid; P_i^{HESS} is the net output power of the HESS; and P_{load} is the electrical load power.

2.3 HESS Modelling Considering Power Supply Demand

(1) HESS Installation Capacity Constraint

The potential capacity of the hybrid energy storage unit is limited, and a balance is struck between investment costs and energy demand to identify the optimal capacity ratio of the hybrid energy storage system.

$$\begin{cases} E_{\text{HESS},i,\min} \leqslant E_{\text{HESS},i} \leqslant E_{\text{HESS},i,\max} \\ E_{HESS,i} = E_{Li,i} + E_{Hy,i} \end{cases} \tag{9}$$

where $E_{\text{HESS},i}$ denotes the installed capacity of the HESS at load point i; $E_{\text{HESS},i,\max}$, $E_{\text{HESS},i,\min}$ represent the upper and lower limits of the installed HESS capacity at load point i, respectively.

(2) HESS Charging and Discharging Power Limit

$$\begin{cases} 0 \leqslant P_{\text{ch}}(t) \leqslant G_{\text{HESS}}(t) P_{\text{ch. max}} \\ 0 \leqslant \eta_{\text{ch}} P_{\text{ch}}(t) \leqslant G_{\text{HESS}}(t) (E_{\text{s. max}} - E_{\text{s}}(t)) \end{cases} \tag{10}$$

$$\begin{cases} 0 \leqslant P_{\text{dis}}(t) \leqslant G_{\text{HESS}}(t) P_{\text{dis,max}} \\ 0 \leqslant P_{\text{dis}}(t) / \eta_{\text{dis}} \leqslant G_{\text{HESS}}(t) (E_{\text{s}}(t) - E_{\text{s,min}}) \end{cases} \tag{11}$$

where $P_{\text{ch}}(t)$ and $P_{\text{dis}}(t)$ represent the charging and discharging power of the HESS at time t, respectively; $P_{\text{ch,max}}$ and $P_{\text{dis,max}}$ denote the upper limits for charging and discharging power at time t, respectively; $G_{\text{HESS}}(t)$ indicates the power supply status of the HESS at time t; η_{ch} and η_{dis} are the charging and discharging efficiencies of the HESS; $E_{\text{s}}(t)$ is the remaining energy of the HESS at time t; $E_{\text{s,max}}$ and $E_{\text{s,min}}$ represent the maximum energy storage capacity and the minimum allowable remaining energy of the HESS, respectively.

(3) HESS SOC Constraint

$$\begin{cases} S_{\text{Li,min}} < S_{\text{Li}} < S_{\text{Li,max}} \\ S_{\text{Hy,min}} < S_{\text{Hy}} < S_{\text{Hy,max}} \end{cases} \tag{12}$$

$$S_{\text{Li}}(t) + \tau \cdot S_{\text{Hy}}(t) \geq \delta_{\text{S}} \tag{13}$$

where $S_{\text{Li,max}}$ and $S_{\text{Li,min}}$ represent the upper and lower limits of the state of charge for the lithium-based energy storage, respectively; $S_{\text{Hy,max}}$ and $S_{\text{Hy,min}}$ denote the upper and lower limits of the state of charge for the hydrogen-based energy storage, respectively; the parameter τ is a conversion coefficient used to equate its state of charge to that of lithium-based storage within a unified optimization framework. With reference to typical modeling approaches for hybrid energy storage systems and considering the differences in their energy density and dynamic response characteristics, this paper adopts $\tau = 0.7$; δ_S represents the joint target for safe system operation, with $\delta_S = 40\%$.

2.4 PV Uncertainty Modeling and Scenario Creation

In the joint planning of HESS and the distribution network, optimal capacity configuration must be considered. It is necessary to account for both the temporal characteristics of PV generation and load, as well as the correlation between PV generation volatility and load. Solar irradiance is assumed to follow a Beta distribution. The output of the PV generation system $P_{\mathrm{PV}}(t)$ is primarily influenced by three factors: solar irradiance $G(t)$, PV panel temperature $T(t)$, and panel characteristic parameters. The PV output model is:

$$P_{\mathrm{PV}}(t) = A \cdot G(t) \cdot \eta_0 \{1 - \beta [T(t) - T_{\mathrm{ref}}]\} \tag{14}$$

where A is the effective area of the PV module, η_0 is the conversion efficiency of the PV panel under standard test conditions, β is the temperature coefficient of the PV panel, and T_{ref} is the standard reference temperature.

Using the probability distributions of PV output and load demand, correlated PV-load scenarios are jointly generated via the Monte Carlo method and then reduced using the K-means algorithm. This joint modeling preserves the temporal correlation between PV generation and load demand observed in the historical data. A total of 500 PV scenarios are created by sampling from the Beta and Normal distributions. The transposed combined PV-generation and load-demand data are clustered into five groups using the K-means algorithm, each containing the associated load and PV output time-series data. Finally, five typical PV generation scenarios are derived using the synchronous back-substitution elimination method. The system is analyzed based on the annual typical day output curves corresponding to these scenarios.

3 Bi-Level Hybrid Energy Storage Optimization Model

3.1 Bi-Level Hybrid Energy Storage Configuration Principles and Architecture

Considering the PV hosting rate, voltage characteristics, and operational economics in distribution network optimization, a bi-level hybrid energy storage optimization configuration model was developed, comprising both single-microgrid optimal capacity configuration and coordinated multi-microgrid global optimization. Its principles and architecture are illustrated in Fig. 4. In this model, feedback from the lower operational level to the upper planning level is realized through a bi-level iterative solution process: candidate configurations from the upper-level planning are evaluated based on the actual performance of the lower-level operation, and the evaluation results directly guide the upper-level planning to update the configuration scheme during iteration, thereby achieving dynamic closed-loop coordination between planning and operation.

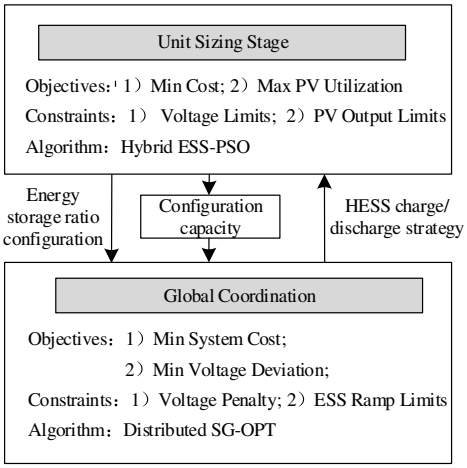

Figure 4: HESS Bi-level optimization configuration model.

The bi-level optimization is realized through a cooperative interaction mechanism between the planning layer and the operation layer. In the upper planning layer, under boundary conditions that satisfy the hosting rate mechanism and power supply requirements, the model determines the optimal capacity configuration of lithium-based and hydrogen-based storage in a locally autonomous manner. This planning scheme is then passed to the lower operation layer. The operation layer further incorporates inter-regional power exchange constraints, improves grid voltage deviation through coordinated dispatch of multi-regional energy storage, and performs global operational optimization by coordinating constraints based on the SOC of the energy storage systems. The operation layer feeds back the actual dispatch performance and voltage indicators to the planning layer, guiding it to adjust the energy storage capacity configuration, thereby preventing over-charging or over-discharging during long-term system operation. Through this closed-loop feedback between planning and operation, the bi-level structure achieves dynamic coordination in both spatial and temporal dimensions, ultimately yielding the optimal configuration and operational strategy for the energy storage system through iterative optimization.

In the proposed bi-level optimization framework, consistency between the planning and operation layers is achieved through a closed-loop interaction across different time scales. The upper layer deter-mines the long-term capacity configuration of the hybrid energy storage system, which serves as the boundary condition for the lower-layer operational optimization. The lower layer simulates short-term dispatch scenarios based on typical daily operation and feeds back critical operational indicators to the upper layer, such as state-of-charge trajectories, voltage deviations, and PV curtailment rates. This feedback mechanism enables the planning layer to evaluate and adjust the capacity configuration ac-cording to actual operational performance, ensuring that investment decisions align with realistic grid dynamics. Consequently, the proposed bi-level model effectively bridges the gap between long-term planning and short-term operation, thereby avoiding over-investment issues caused by time-scale mismatches.

3.2 Single-Microgrid Optimal Capacity Configuration Model

3.2.1 Objective Function of the Optimal Capacity Configuration Model for a Single Microgrid

(1) Minimise cost

The aim is to minimise the hybrid energy storage investment cost C_{HESS}, operation and maintenance cost C_{MA}, and system PV generation cost C_{PV}, reaching a local minimum.

$$f_1 = \min\left(C_{\mathrm{HESS}} + C_{\mathrm{MA}} + C_{\mathrm{PV}}\right) \tag{15}$$

$$C_{\mathrm{MA}} = \varepsilon \cdot c_{\mathrm{MA}}^{Hy} \cdot E_{\mathrm{Hy}} + (1-\varepsilon) \cdot c_{\mathrm{MA}}^{Li} \cdot E_{\mathrm{Li}} \tag{16}$$

where ε lithium battery proportion in the HESS; E_{Hy}, and E_{Li} represent the annual total operating electricity of the hydrogen and lithium batteries, respectively; c_{MA}^{Hy} and c_{MA}^{Li} represent the unit maintenance cost of hydrogen-based and lithium-based batteries, respectively.

Among them, C_{HESS} comprises the daily investment cost of the HESS, C^{INV}, and its operational cost, C^{OP}.

$$C_i^{\mathrm{INV}} = \sum_{i=1}^{n_{\mathrm{ESS}}} \left(\alpha_{\mathrm{Li},i} E_{\mathrm{Li},i} + \beta_{\mathrm{Li},i} P_{\mathrm{Li},i} + \alpha_{\mathrm{Hy},i} E_{\mathrm{Hy},i} + \beta_{\mathrm{Hy},i} P_{\mathrm{Hy},i}\right) \tag{17}$$

$$C_{i,j,t}^{\mathrm{OP}} = P_{i,j,t}^{\mathrm{HESS}} \cdot c_{i,j,t}^{\mathrm{OP}} \tag{18}$$

where: n_{ESS} is the number of HESS units; $P_{\mathrm{Li},i}$ and $P_{\mathrm{Hy},i}$ are the power ratings of the lithium-based and hydrogen-based energy storage within the i-th HESS, respectively; α_i and β_i are the unit capacity cost and unit power cost of the i-th energy storage system, respectively; $c_{i,j,t}^{\mathrm{OP}}$ is the unit operational cost.

And $\mathrm{C_{PV}}$ comprises the operating cost $C^{\mathrm{OP,PV}}$, and the maintenance cost $C^{\mathrm{MA,PV}}$ of PV power generation, with its specific expression as follows:

$$C_{\mathrm{PV}} = \sum_{i=1}^{N_{\mathrm{MG}}} \sum_{j=1}^{N_{\mathrm{PV},i}} \sum_{t=1}^{T} \left[C_{i,j,t}^{\mathrm{OP,PV}} + C_{i,j,t}^{\mathrm{MA,PV}} \right] \tag{19}$$

$$C_{i,j,t}^{\mathrm{OP,PV}} = P_{i,j,t}^{\mathrm{PV}} \times c_{i,j,t}^{\mathrm{OP,PV}} \tag{20}$$

$$C_{i,j,t}^{\mathrm{MA,PV}} = P_{i,j,t}^{\mathrm{PV}} \times c_{i,j,t}^{\mathrm{MA,PV}} \tag{21}$$

where N_{MG} is the number of microgrids, $N_{\mathrm{PV},i}$ is the number of connected photovoltaic units, and T is the time; $c_{i,j,t}^{\mathrm{OP,PV}}$ is the unit power operational cost of PV generation for unit j in microgrid i at time t, which includes equipment depreciation; $c_{i,j,t}^{\mathrm{MA,PV}}$ is the maintenance cost of PV generation for the same unit, covering labor, routine maintenance, and repair expenses. Summary of Cost Components and Units is shown in Table 1.

Table 1: Summary of cost components and units.

Cost Component	Symbol	Unit
Hybrid Energy Storage System Investment Cost	C_{HESS}	CNY
Operation and Maintenance Cost of HESS	C_{MA}	CNY/year
PV Generation Cost	C_{PV}	CNY
Investment Cost of HESS Unit i	C_i^{INV}	CNY
Operational Cost of HESS	$C_{i,j,t}^{\mathrm{OP}}$	CNY
Operational Cost of PV	$C_{i,j,t}^{\mathrm{OP,PV}}$	CNY
Maintenance Cost of PV	$C_{i,j,t}^{\mathrm{MA,PV}}$	CNY
Unit Capacity Cost of Energy Storage	α_i	CNY/kWh
Unit Power Cost of Energy Storage	β_i	CNY/kW

(2) Maximum photovoltaic consumption rate

$$f_2 = \mathrm{Max} \sum_{i=1}^{N_{\mathrm{MG}}} \sum_{t}^{T} \left[P_{\mathrm{PV},i,t}^{\mathrm{ref}} - P_{\mathrm{PV,un},t} \right] \tag{22}$$

$$P_{\mathrm{PV,un},t} = \max\left\{0, P_{m,t} - P_{\mathrm{load},t}\right\} \tag{23}$$

$$P_{\mathrm{load},t} = P_{\mathrm{load},m,t} + C_{\mathrm{HESS}} \times E \tag{24}$$

where $P_{m,t}^{\mathrm{load}}$ denotes the load demand of microgrid m; $P_{m,t}$ represents the photovoltaic power generation of microgrid m, $P_{\mathrm{load},t}$ is the adjusted load demand, which includes the supplementation of the load by the energy storage capacity; $P_{\mathrm{pv,un},t}$ represents the unconsumed PV power. $P_{\mathrm{PV},i}^{\mathrm{ref}}$ denotes the available PV power in microgrid i at time t; E represents the charge and discharge efficiency, which is 90%; C_{HESS} denotes the capacity of the hybrid energy output.

(3) Multi-objective optimisation problem handling

Adopt the linear weighting method, adjusting the influence of various objectives in a multi-objective optimisation problem by assigning weight coefficients.

$$f = \xi_1 f_1 - \xi_2 f_2 \tag{25}$$

In the equation, ξ_1 and ξ_2 are the weighting coefficients, with ξ_1 set at 0.7 and ξ_2 at 0.3 as determined through sensitivity analysis, as shown in Table 2. The weight values are selected to achieve a balanced compromise on the Pareto frontier between minimizing cost and maximizing PV utilization. Within a reasonable range around these values, the final system configuration and key performance indicators remain stable.

Table 2: Optimization results under different weight coefficient combinations.

Case	ξ_1	ξ_2	Total Cost (10^4 CNY)	PV Utilization (%)
1	0.5	0.5	612.3	93.8%
2	0.7	0.3	585.5	96.2%
3	0.9	0.1	568.7	90.5%

As presented in Table 2, the allocation of weight coefficients significantly affects both the total system cost and the PV utilization rate. In Case 1, where equal importance is assigned to economic performance and renewable energy accommodation, the system achieves a balanced trade-off, with a total cost of 612.3×10^4 CNY and a PV utilization rate of 93.8%. In Case 2, which emphasizes cost reduction while maintaining moderate consideration for PV integration, the total cost decreases to 585.5×10^4 CNY, while the PV utilization rate increases to 96.2%. This indicates that an appropriately weighted cost objective can effectively encourage energy storage utilization without compromising economic efficiency. In Case 3, where cost minimization is strongly prioritized, the total cost is further reduced to 568.7×10^4 CNY; however, the PV utilization rate declines to 90.5%. This decline reflects the underutilization of energy storage for renewable energy accommodation under stringent cost constraints.

3.2.2 Constraints in the Single Microgrid Optimization Stage

(1) Node voltage constraints

$$U_{\min} \le U_i(t) \le U_{\max} \tag{26}$$

where $U_{\max}$ and $U_{\min}$ represent the upper and lower limits of the node voltage, respectively.

(2) PV generation output constraints

$$0 \leqslant P_{\mathrm{PV}}(t) \leqslant P_{\mathrm{PV,max}} \tag{27}$$

where $P_{\mathrm{PV}}(t)$ denotes the output power of the PV system at time t; $P_{\mathrm{PV,max}}$ is the upper limit of the PV output power at time t.

3.2.3 Solution Methods for the Optimisation Model of a Single Microgrid

The HESS capacity configuration model, which aims to maximise renewable energy utilisation, takes minimizing the cost of a single microgrid as the optimization objective. Considering the node voltage

constraints of the high-penetration PV grid-connected system and the output constraints of PV units, the optimal hybrid energy storage configuration capacity for a single microgrid is derived using the MA that coordinates multiple energy storage technologies.

During the spatial initialization operation, two groups of mayfly individuals are generated, representing male and female populations, respectively. In the algorithm, each mayfly's position is represented by a d-dimensional vector $M = [m_1, m_2 \cdots m_d]$, serving as a potential solution to the problem. The fitness of each mayfly is evaluated through the objective function to assess the quality of its solution. The velocity of each mayfly is defined as $V = [v_1, v_2 \cdots v_d]$. Mayflies adjust their flight direction based on their individual historical best p_{best} and the global best of the population g_{best}, thereby updating their position and velocity. In Eq. (29), the first term gv_z^t represents the inertia component, which retains the previous velocity; the second term $c_1 e^{-\beta r_p^2}$ signifies individual cognition, driving the mayfly toward its own historical best position; and the third term $c_2 e^{-\beta r_g^2}$ denotes social cognition, guiding it toward the global best position of the population. The algorithm iterates until either a preset maximum number of iterations is reached or the solution quality meets the convergence criteria.

Male mayflies update their positions according to the distance between themselves and nearby mayflies, as described by the formula:

$$m_z^{t+1} = m_z^t + v_z^{t+1} \tag{28}$$

$$v_z^{t+1} = gv_z^t + c_1 e^{-\beta r_p^2} \left(p_{best,z} - m_z^t\right) + c_2 e^{-\beta r_g^2} \left(g_{best,z} - m_z^t\right) \tag{29}$$

where m_z^t is the position of the z-th male mayfly at time t; v_z^{t+1} is the velocity of the z-th mayfly at time $t+1$; c_1 is the weight coefficient for individual learning; c_2 is the weight coefficient for social learning; g represents the gravity coefficient; β is the visibility coefficient; r_g is the Cartesian distance between the current position and $p_{best,z}$; r_p is the Cartesian distance between the current position and $g_{best,z}$.

Female mayflies are processed by sorting both male and female mayflies in descending order of their individual fitness function values. Consequently, the top-ranked female mayfly is attracted to the top-ranked male mayfly, the second-ranked female mayfly to the second-ranked male mayfly, and so on. The formula is as follows:

$$v_z^{t+1} = \begin{cases} gv_z^t + c_2 e^{-\beta r_{mf}^2} \left(m_z^t - f_z^t\right), F\left(m_z^t\right) < F\left(f_z^t\right) \\ gv_z^t + \xi, F\left(m_z^t\right) > F\left(f_z^t\right) \end{cases} \tag{30}$$

$$f_z^{t+1} = f_z^t + v_z^{t+1} \tag{31}$$

where r_{mf} is the distance between the male and female mayflies; ξ is the random flight coefficient; F is the objective function; f_z^t is the position of the female mayfly at time t; v_z^{t+1} is the velocity at time $t+1$.

Finally, the mating operation is performed for all corresponding mayfly pairs. Each mating produces two offspring, calculated as follows:

$$\begin{cases} P1 = \gamma \cdot x_{male} + (1-\gamma) \cdot y_{female} \\ P2 = \gamma \cdot y_{female} + (1-\gamma) \cdot x_{male} \end{cases} \tag{32}$$

In the formula: $P1$ and $P2$ are the two new offspring produced after mayfly mating; γ is a random number within the range $[0, 1]$, representing the gene crossover ratio.

3.3 Globally Coordinated Multi-Microgrid Optimization Configuration

3.3.1 Objective Function of the Globally Coordinated Optimal Configuration Model for Multi-Microgrids

The voltage at each node of the distribution network must be kept within a certain range, and its fluctuations should stay minimal. The improvement of node voltage is described by the reduction in node voltage deviation before and after the optimal configuration of the HESS. The model is expressed as follows.

$$f_3 = \min \sum_{t=1}^{24} \sum_{i \in \Omega} \left(\frac{\left| U_{t.i}^{(1)} - U_{\mathrm{N}} \right|}{U_{\mathrm{N}}} - \frac{\left| U_{t.i}^{(0)} - U_{\mathrm{N}} \right|}{U_{\mathrm{N}}} \right) \tag{33}$$

where Ω denotes the set of nodes in the distribution network; $U_{t.i}^{(0)}$ and $U_{t.i}^{(1)}$ represent the voltage before and after the optimal configuration of the HESS, respectively. U_{N} is the rated voltage.

Minimising the global cost

This calculates the total cost in distributed optimisation under probability-weighted scenarios, including photovoltaic generation, load demand, energy storage output, and related costs. By adding voltage penalty and voltage stability weighting coefficients, it partly considers the effect of voltage limit violations on costs. The specific formula is as follows:

$$f_4 = \min \left[C_{\mathrm{gen}}^{\mathrm{d}} + C_{\mathrm{MA}}^{\mathrm{d}} + C_{ex} + U_{\mathrm{p}} U_{\mathrm{st}} \right] \tag{34}$$

where $C_{\mathrm{gen}}^{\mathrm{d}}$ is the grid electricity purchase cost; $C_{\mathrm{MA}}^{\mathrm{d}}$ is the maintenance cost of the energy storage devices across multiple areas; C_{ex} is the interaction cost between microgrids; U_{p} is the voltage penalty value; U_{st} is the voltage stability weighting coefficient.

The specific expressions for the grid purchase cost and the maintenance cost of multi-microgrid energy storage devices are as follows:

$$C_{\mathrm{gen,d}} = 0.5 \sum_{m}^{M} \sum_{t}^{T} P_{m,t}^{\mathrm{grid}} \tag{35}$$

$$C_{\mathrm{MA,d}} = 0.1 \sum_{m}^{M} \sum_{t}^{T} \left| S_{m,t}^{\mathrm{d}} \right| \tag{36}$$

$$P_{m,t}^{\mathrm{grid}} = \max \left[0, P_{m,t}^{\mathrm{load}} - P_{m,t} - S_{m,t}^{\mathrm{d}} \right] \tag{37}$$

where $P_{m,t}^{\mathrm{grid}}$ denotes the grid power supply to the m-th microgrid at time t. Eq. (37) ensures, through the action of PV and energy storage devices, that $P_{m,t}^{\mathrm{grid}}$ does not take negative values, indicating that microgrids are not allowed to sell power back to the main grid; $S_{m,t}^{\mathrm{d}}$ represents the total output of all energy storage devices in microgrid m at time t.

The inter-microgrid interaction cost consists of the line loss cost and the equipment degradation cost.

$$C_{ex} = C_{loss} + C_{de} \tag{38}$$

$$C_{loss} = \sum_{t=1}^{T} \sum_{l=1}^{L} \left(I_l^2(t) \cdot R_l \cdot \Delta t \cdot \pi_{loss} \right) \tag{39}$$

$$C_{de} = \alpha_1 \cdot \sum_{t=1}^{T} \left(\frac{\sum_{i \neq j} \left| P_{ij}(t) \right|}{S_{rated}} \right)^{\beta_1} \cdot C_{dep} \tag{40}$$

where $I_l\ (t)$ is the current of the tie line; R_l is the resistance of the tie line; π_{loss} is the unit loss electricity price; α_1 is the equipment type coefficient; S_{rated} is the rated capacity of the equipment; β_1 is the loss exponent; C_{dep} is the equipment depreciation cost.

3.3.2 Constraints in the Coordination Optimisation Stage of Multi-Microgrids

(1) Voltage penalty constraint

$$U_p = \begin{cases} (U_{\min} - U)^2, & U < U_{\min} \\ (U - U_{\max})^2, & U_{\max} < U \\ 0, & U_{\min} < U < U_{\max} \end{cases} \tag{41}$$

(2) Power interaction constraint

In a multi-microgrid energy storage system, the inter-regional power flow and interactions must satisfy constraint conditions to ensure reasonable node voltages and improve PV consumption capacity. Let P_{ij} be the power flow between microgrid i and j; the power interaction constraint can be expressed as:

$$P_{ij}\ (t) \le P_{ij}^{\max}, \forall t, i, j \tag{42}$$

3.3.3 Solution Approach for the Multi-Microgrid Coordinated Optimisation Model

In the second stage, the SGD method is employed for global multi-microgrid distributed optimisation. Based on local optimisation of each energy storage unit, SGD facilitates information coordination and sharing among units. When combined with the multi-microgrid CIDS system, SGD helps smooth power fluctuations, coordinates energy storage and photovoltaic units, and maintains global operational balance and economic optimality of the grid. In SGD, each node calculates the gradient and sends it to a randomly chosen node; this node updates the model parameters accordingly and then passes them to other nodes, repeating the process until convergence. The aim is to find parameters that minimise the objective function $J(\theta)$, with the multi-objective handling method remaining the same as in the first stage.

3.4 Model Solving Process

The bi-level model is solved using a combined MA and SGD approach. Here, m and M denote the iteration counts set for the upper-level planning model and the lower-level operation model, respectively. The upper-level planning leverages the cooperation and competition mechanisms of the MA to rapidly search for the optimal HESS capacity configuration within the local microgrid. The lower-level operation iteratively updates the global SOC parameters of the energy storage systems to address multi-regional information sharing and dynamic game problems. The specific solution steps are as follows:

(1) Step 1: Perform upper-level optimization. Initialize MA parameters and set the maximum number of iterations.
(2) Step 2: Initialize MA positions and velocities. The particle position represents the HESS capacity and power configuration.
(3) Step 3: Optimize the particle population (i.e., HESS capacity configurations) with the objectives of minimizing HESS system operating costs and maximizing the PV utilization rate.
(4) Step 4: Transfer the HESS capacity configuration results obtained from the upper-level planning to the lower-level operation optimization model.
(5) Step 5: Set parameters such as the learning rate, randomly generate training samples, and solve the loss function.

(6) Step 6: Using the SGD algorithm and aiming to minimize the total system cost, update the global optimal solution based on the SOC and power flow results until the iteration stopping criteria are met.
(7) Step 7: Adjust the charging/discharging states of each microgrid by updating their energy storage SOC. Feed the lower-level operation results back to the upper level to adjust the local microgrid capacity configuration.
(8) Step 8: Calculate the objective function value by combining the local and global optimization results. If the convergence criteria are satisfied, stop the iteration and output the optimal solution; otherwise, return to Step 5.

4 Simulation Verification

4.1 Case Study Introduction

To verify the effectiveness of the proposed method, a 33-bus system based on real grid data is constructed for analysis, combining the operating conditions of an actual regional power grid in Zhejiang with the IEEE 33-bus system structure. The system base voltage is 10.5 kV, and the total network load is 3840 + j2315 kV A. In the MA, the population size is 50, and the maximum number of iterations is 100. In the SGD algorithm, the maximum number of iterations is 100, and the learning rate is 0.01. The optimisation model is built and simulated in MATLAB R2023b. The location and capacity of PV installations influence the voltage and losses of the distribution network.

4.2 Simulation Results Analysis

Microgrid systems with an installed capacity of 1 MW PV are connected at nodes 6, 18, 22, and 33, as shown in Fig. 5 The following schemes are considered:

(1) Scheme 1: Optimise the configuration using the proposed two-stage HESS model.
(2) Scheme 2: Local optimisation only, without considering the coordination mechanism among multiple microgrids.
(3) Scheme 3: No algorithmic or global coordination assistance; directly configure the HESS.

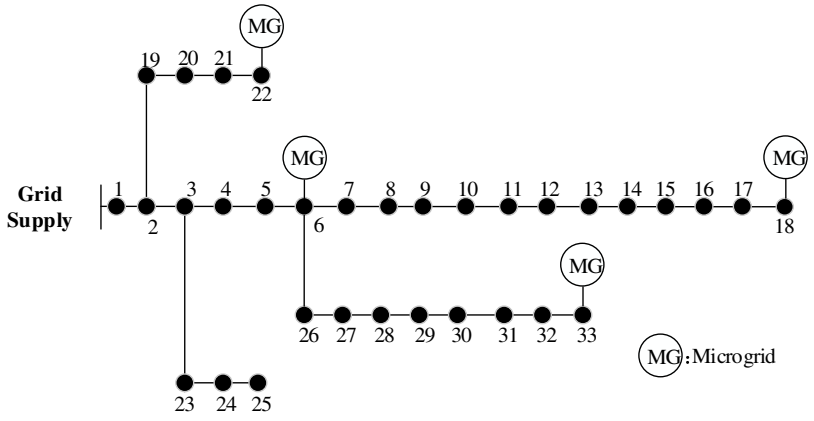

Figure 5: Construct a 33-Bus distribution network topology diagram.

The total cost, PV utilisation rate, voltage violation duration, and microgrid power exchange for the three schemes are summarized in Table 3. The efficiency curves of the electrolyzer and fuel cell are shown in Fig. 6. For comparative analysis, the scenario without energy storage is included as a benchmark in Fig. 7. The optimal hybrid energy storage configuration for Scheme 1 is provided in Table 4. Under this

configuration, voltage fluctuations are minimised, the total system cost is the lowest, and PV utilisation is maximised.

Table 3: System results for the optimal configuration.

Scenario	Total Cost (10^4 CNY)	PV Utilization(%)	Voltage Violation (h/d)	Microgrid Power (MWh/d)
1	585.5	96.2%	0.28	48.1
2	796.8	88.3%	1.61	0
3	692.4	80.1%	4.20	20.7

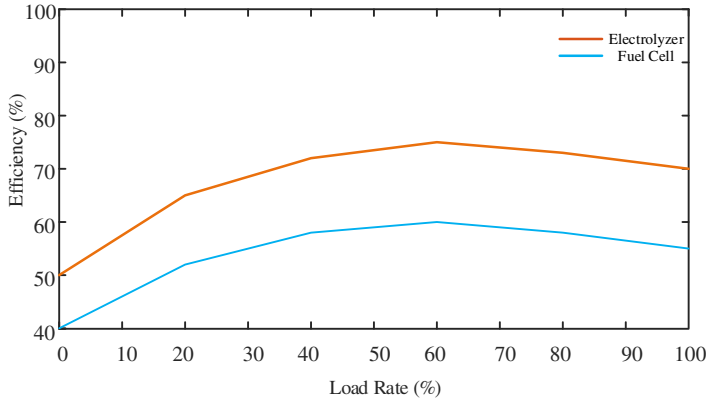

Figure 6: Efficiency curves of key equipment in hydrogen energy storage system.

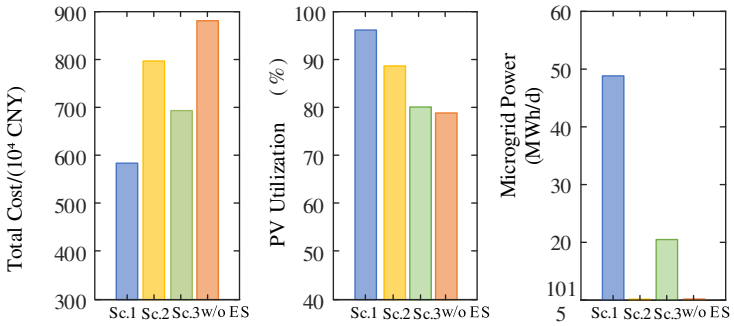

Figure 7: Comparison of simulation results.

Table 4: Optimal hybrid energy storage configuration.

Installation Node	Lithium ESS/(MW·h)	Hydrogen ESS/(MW·h)
6	0.268	0.442
18	0.339	0.587
22	0.220	0.475
33	0.394	0.496

From the different optimisation results in Table 3, it is evident that among the three schemes. For Scheme 1, the first stage employs the MA for local microgrid optimization. It accurately configures the capacity of each energy storage unit, while fully considering both investment and operating costs of storage equipment. This allows the PV power utilization rate to reach its maximum. In the second stage, Scheme 1 utilises the SGD algorithm for global optimisation and information coordination. This process effectively integrates the energy scheduling of all storage units, and the power interaction mechanism enables the system to maintain both flexibility and economic efficiency. As a result, both the scheduling cost of the grid and the operating cost of the storage system are reduced. Through power interaction and global coordination among multiple microgrids, the dispatch strategy of storage units can be swiftly adjusted, ultimately achieving global optimisation.

In Scheme 2, only local optimisation is carried out, and it does not account for the coordination between microgrids, which results in a local optimum. In this scheme, more storage units are installed at multiple nodes, leading to higher investment and maintenance costs. Compared to Scheme 3, Scheme 2 can attain a better PV utilisation rate through local optimisation. However, it limits storage capacity to cut investment costs, which causes a lower utilisation rate than Scheme 1. Additionally, due to the absence of coordination, Scheme 2 cannot achieve energy complementarity across microgrids, resulting in a lower overall utilisation rate.

In Scheme 3, the storage capacity is minimised through empirical configuration, resulting in a lower total cost than Scheme 2. However, the traditional configuration approach in Scheme 3 is inadequate in terms of grid performance. It does not effectively balance the configuration and scheduling of storage units, leading to the lowest PV utilisation rate. Scheme 3 shows that simple rules cannot address the complex coordination challenges of multi-microgrid systems. While basic coordination functions are feasible, it lacks state awareness, dynamic decision-making, and forecasting capabilities.

Fig. 8 shows the daily dispatch schedule and SOC of the HESS. As shown, the lithium-based energy storage, with its fast response and high charge/discharge frequency, mitigates short-term, frequent power fluctuations. In contrast, the hydrogen-based energy storage, characterized by its large capacity, is employed for long-duration regulation, resulting in a smoother SOC profile. Throughout the 24-h period, both lithium and hydrogen storage systems operate normally: they release energy when the system equivalent load is high and absorb energy when the load is low, thereby ensuring stable system operation while maintaining their respective SOC within the normal range of 10% to 90%.

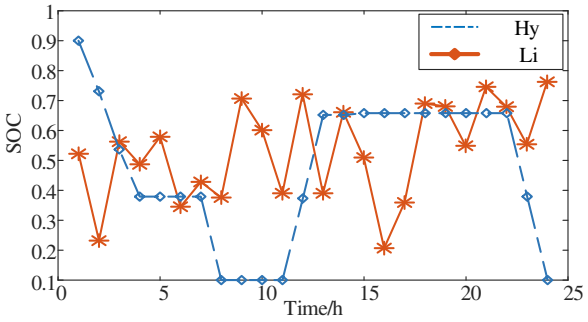

Figure 8: SOC profiles of lithium-based and hydrogen-based energy storage systems.

Additionally, the proposed two-stage optimisation model effectively enhances voltage quality. Fig. 9 compares the voltage magnitudes for the three schemes and the case without energy storage, with annotations indicating the voltage fluctuation standard deviation σv and the voltage increase for each scheme. Simulation

results indicate that Scheme 1 delivers the best voltage boosting performance, exhibiting the smallest overall and inter-node voltage fluctuation. Using MA optimisation, Scheme 1 ensures each storage unit operates efficiently within the grid, preventing excessive voltage swings; meanwhile, the SGD algorithm coordinates the entire grid, facilitating collaborative operation among multi-regional storage units and maintaining voltage magnitudes within the range [0.96, 1.05].

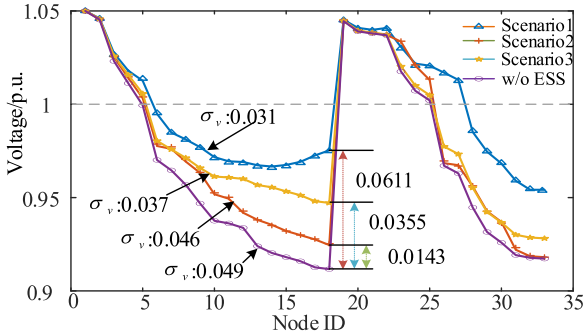

Figure 9: Voltage variation curves for four different schemes.

4.3 Comparative Analysis of Different Energy Storage Technologies

To further investigate how energy storage technology types affect the performance of high-PV-penetration distribution networks, this section establishes the following three comparative schemes based on the verified bi-level optimization framework. Their mathematical formulation is identical to that presented in Section 4.2, aiming to reveal the intrinsic characteristics and synergistic value of different storage technologies:

(1) Scheme 4: Optimise the configuration using the proposed two-stage HES model.
(2) Scheme 5: Local optimisation only, without considering the coordination mechanism among multiple microgrids.
(3) Scheme 6: No algorithmic or global coordination assistance; directly configure the HES.

Significant differences in PV hosting performance are evident among the three schemes, as shown in Fig. 10. Scheme 6 demonstrates the best hosting capability. The key lies in the coordinated operation between the lithium battery and the hydrogen storage: the lithium battery, leveraging its fast power response, prioritises suppressing minute-level fluctuations in PV output; meanwhile, the hydrogen storage, utilising its large capacity, undertakes energy shifting and storage on an hourly or longer timescale. Their complementary roles in the control timeline significantly reduce PV curtailment during midday output peaks. Scheme 5 ranks second in hosting rate. Its large-capacity configuration effectively alleviates the temporal mismatch between PV generation and load demand, making it particularly suitable for absorbing surplus PV energy lasting several hours. However, its limited power regulation rate makes it difficult to fully track power fluctuations caused by sudden changes in solar irradiance. Scheme 4 exhibits the lowest hosting rate. Although the lithium battery possesses excellent transient response capability to effectively track second-level PV fluctuations, its limited energy capacity often leads to prematurely reaching the upper SOC limit during periods of sustained high irradiation. This prevents the storage of subsequent PV output, creating a hosting bottleneck.

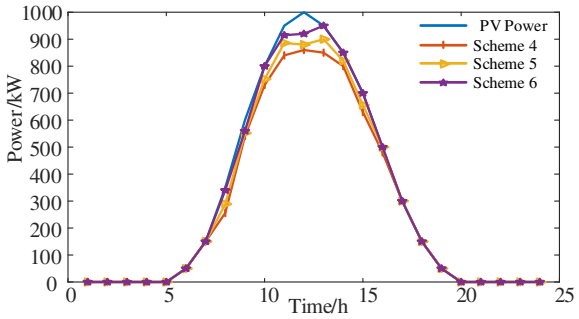

Figure 10: Comparative analysis of PV hosting performance among the three schemes.

Fig. 11 further illustrates the peak-shaving and valley-filling effects of the three schemes. Scheme 6 achieves multi-timescale load smoothing through coordinated lithium and hydrogen storage: the lithium battery responds to rapid load changes and PV fluctuations, while the hydrogen storage provides sustained energy support over several hours, thereby significantly reducing the daily load peak-to-valley difference. Scheme 5 performs well in long-timescale peak-shaving and valley-filling, effectively shifting midday PV surplus to the evening peak period. However, its limited power regulation rate restricts its ability to suppress short-term load spikes. Scheme 4, despite excellent dynamic regulation for suppressing instantaneous load fluctuations, lacks sufficient energy endurance to support periods of high load or PV surplus lasting several hours. The comparison indicates that in high-penetration PV integration scenarios, a hybrid energy storage system, by coordinating power-type and energy-type storage technologies, can not only enhance the PV hosting level but also improve the net load characteristics across multiple timescales, thereby increasing the flexibility and stability of grid operation.

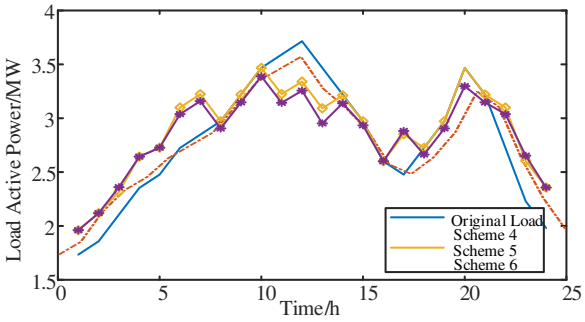

Figure 11: Comparative analysis of peak-shaving and valley-filling effects among the three schemes.

4.4 Parameter Sensitivity Analysis

To validate and optimize the performance of the adopted MA, this section conducts a sensitivity analysis of its key parameter—the population size (PopSize). Scenarios with population sizes of 30, 40, 50, and 60 were tested. By comparing the optimization results across these parameter settings, the variation in the objective function value with the number of iterations during the optimization process is recorded, as shown in Fig. 12.

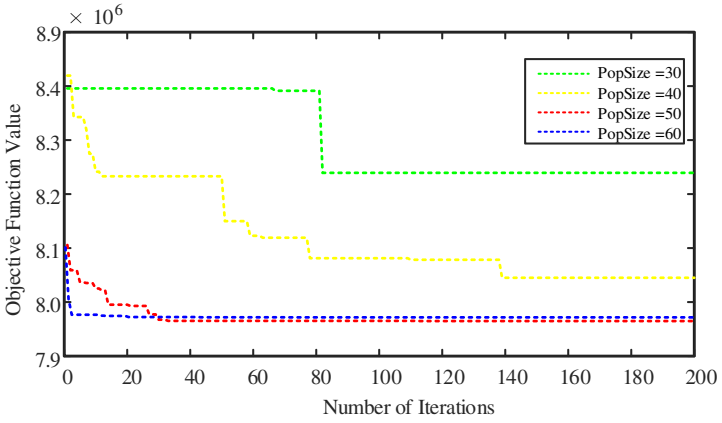

Figure 12: Comparison of convergence curves for different population sizes.

As shown in the figure, smaller population sizes exhibit lower optimization efficiency in later stages, resulting in a higher final convergence value. However, a larger population size, such as 60, achieves the fastest convergence speed, yet its final convergence value is not optimal. Considering convergence speed, stability, and computational efficiency collectively, a population size of 50 is identified as the optimal parameter setting for the MA algorithm in this case study. It ensures rapid, stable, and deep convergence at an acceptable computational cost, providing a reliable foundation for the proposed bi-level optimization model in this paper.

5 Conclusion

Addressing node voltage violations and limited PV hosting capacity arising from high-penetration PV integration in distribution networks, this paper establishes a bi-level HESS optimization configuration model. This model is integrated with the distribution network to determine the optimal locations and capacities for energy storage deployment, thereby forming an optimized configuration framework for distribution networks with high PV penetration and distributed hybrid storage. Case studies verify the feasibility and effectiveness of the proposed bi-level optimization model. The main conclusions are as follows:

(1) The bi-level optimization configuration method fully utilizes the strengths of the MA and SGD. It achieves a cost reduction of 15.44%, increases the PV hosting rate from 80.1% to 96.2%, and leads to a marked improvement in mitigating voltage violations.

(2) The closed-loop interaction between local autonomous optimization and global coordination, facilitated by dynamic parameter exchange, effectively links “planning” with “operation”. The incorporation of a multi-microgrid interaction mechanism enhances the system’s hosting capacity and resilience, thereby improving grid economy, operational efficiency, and the utilization efficiency of renewable energy.

(3) The flexible and adaptive configuration of the lithium-hydrogen hybrid energy storage enhances the system’s ability to accommodate fluctuations from both the grid and load demand, resulting in a significant reduction in the daily load peak-to-valley difference.

Acknowledgement: The authors thank the Northeast Electric Power University for conducting this research.

Funding Statement: This work was supported in part by State Grid Corporation of China Headquarters Technology Project (5100-202340815A-3-8-KJ).

Author Contributions: Yechun Xin and Xinxin Cheng wrote the main manuscript text, Yanxu Wang and Weiru Wang prepared figures, Jiexiang Han and Zhen Niu prepared tables. All authors reviewed and approved the final version of the manuscript.

Availability of Data and Materials: Due to the nature of this research, participants of this study did not agree for their data to be shared publicly, so supporting data is not available.

Ethics Approval: Not applicable.

Conflicts of Interest: The authors declare no conflicts of interest.

References

1. Yu X, Yang K. Distribution network optimization model of industrial park with distributed energy resources under the carbon neutral targets. Energy Eng. 2023;120(12):2741–60. doi:10.32604/ee.2023.028041.
2. Ding Z, Xiang Q, Li C, Ma M, Zhang C, Gu X, et al. Dynamic boundary optimization via IDBO-VMD: a novel power allocation strategy for hybrid energy storage with enhanced grid stability. Energy Eng. 2026;123(1):1–10. doi:10.32604/ee.2025.070442.
3. Wang S, Yue Y, Cai S, Li X, Chen C, Zhao H, et al. A comprehensive survey of the application of swarm intelligent optimization algorithm in photovoltaic energy storage systems. Sci Rep. 2024;14(1):17958. doi:10.1038/s41598-024-68964-w.
4. Nassar SM, Saleh AA, Eisa AA, Abdallah EM, Nassar IA. Optimal planning of integrated nuclear-hybrid renewable energy systems for electrical distribution networks based on artificial intelligence. Sci Rep. 2025;15(1):26004. doi:10.1038/s41598-025-11049-z.
5. Nguyen-Tuan A, Ta-Duy B, Nguyen-Duc T, Fujita G. A novel approach to optimize and allocate battery energy storage system in distributed grid considering impact of demand response program. Sustain Energy Grids Netw. 2025;43(3):101738. doi:10.1016/j.segan.2025.101738.
6. Kang K, Jia H, Hui H, Liu D. Two-stage optimization configuration of shared energy storage for multi-distributed photovoltaic clusters in rural distribution networks considering self-consumption and self-sufficiency. Appl Energy. 2025;394:126174. doi:10.1016/j.apenergy.2025.126174.
7. Manjula A, Kute UT, Reddy CVK, Mallala B. Power quality improvement of microgrid for photovoltaic ev charging station with hybrid energy storage system using RPO-ADGAN approach. J Energy Storage. 2025;108(5):114970. doi:10.1016/j.est.2024.114970.
8. Liu X, Zhao P, Qu H, Liu N, Zhao K, Xiao C. Optimal placement and sizing of distributed PV-storage in distribution networks using cluster-based partitioning. Processes. 2025;13(6):1765. doi:10.3390/pr13061765.
9. Xu Z, Tang Z, Chen Y, Liu Y, Gao H, Xu X. Optimal robust allocation of distributed modular energy storage system in distribution networks for voltage regulation. Appl Energy. 2025;388(4):125625. doi:10.1016/j.apenergy.2025.125625.
10. Cai J, Wang K, Cheok AD, Yan Y. Optimal configuration for power grid battery energy storage systems based on payload fluctuation guided multi-objective PSO. J Energy Storage. 2025;105(6):114515. doi:10.1016/j.est.2024.114515.
11. Elseify MA, Kamel S, Nasrat L. An improved moth flame optimization for optimal DG and battery energy storage allocation in distribution systems. Clust Comput. 2024;27(10):14767–810. doi:10.1007/s10586-024-04668-0.
12. Kamel S, Abdel-Mawgoud H, Alrashed MM, Nasrat L, Elnaggar MF. Optimal allocation of a wind turbine and battery energy storage systems in distribution networks based on the modified BES-optimizer. Front Energy Res. 2023;11:1100456. doi:10.3389/fenrg.2023.1100456.
13. Ma L, Wang K, Chen L, Yu H, Qiao J. Optimized configuration scheme of relay protection for compressed air energy storage system. J Phys Conf Ser. 2025;3046(1):012002. doi:10.1088/1742-6596/3046/1/012002.
14. Meng Q, He Y, Hussain S, Lu J, Guerrero JM. Optimized energy storage configuration for enhanced flexibility in renewable-integrated power systems. J Energy Storage. 2025;132(1):117735. doi:10.1016/j.est.2025.117735.

15. Ghaffari A, Askarzadeh A, Fadaeinedjad R. Optimal allocation of energy storage systems, wind turbines and photovoltaic systems in distribution network considering flicker mitigation. Appl Energy. 2022;319(2):119253. doi:10.1016/j.apenergy.2022.119253.
16. Wu X, Liu Z, Tian L, Ding D, Chen Z. Optimal capacity configuration method for photovoltaic and energy storage in standalone photovoltaic systems. Power Syst Technol. 2014;38(5):1271–76. doi:10.13335/j.1000-3673.pst.2014.05.022.
17. Tao Q, Sang BY, Ye JL, Xue JH. Optimal configuration method of distributed energy storage systems in distribution network with high penetration of photovoltaic. High Volt Eng. 2016;42(7):2158–65. (In Chinese). doi:10.1109/spec.2016.7846051.
18. Lu J, Zheng W, Yu Z, Xu Z, Jiang H, Zeng M. Optimizing grid-connected multi-microgrid systems with shared energy storage for enhanced local energy consumption. IEEE Access. 2024;12(4):13663–77. doi:10.1109/ACCESS.2024.3351855.
19. Wang G, Wang C, Feng T, Wang K, Yao W, Zhang Z. Day-ahead and intraday joint optimal dispatch in active distribution network considering centralized and distributed energy storage coordination. IEEE Trans Ind Appl. 2024;60(3):4832–42. doi:10.1109/TIA.2024.3372943.
20. Yang XH, Yuan ZX, Xiao JY, Wen QW, Zeng JP, Wan ZR. Optimal configuration of hybrid energy storage microgrid considering battery life. Power Syst Prot Control. 2023;51(4):22–31. (In Chinese).